The Journal of Chemical Physics

ARTICLE

pubs.aip.org/aip/jcp

Contribution of piezoelectric effect on piezo-phototronic coupling in ferroelectrics: A theory assisted experimental approach on NBT

Cite as: J. Chem. Phys. 161, 184711 (2024); doi: 10.1063/5.0227731
Submitted: 10 July 2024 • Accepted: 27 October 2024 •
Published Online: 12 November 2024

View Online Export Citation CrossMark

Koyal Suman Samantaray,[1] Sourabh Kumar,[1] Maneesha P,[1] Dilip Sasmal,[1] Suresh Chandra Baral,[1] B. R. Vaishnavi Krupa,[2] Arup Dasgupta,[2] A. Mekki,[3,4] K. Harrabi,[3,5] and Somaditya Sen[1,a)]

AFFILIATIONS

[1] Department of Physics, Indian Institute of Technology Indore, Indore 453552, India
[2] Physical Metallurgy Division, Indira Gandhi Centre for Atomic Research, HBNI, Kalpakkam, Tamil Nadu 603102 India
[3] Department of Physics, King Fahd University of Petroleum and Minerals, Dhahran 31261, Saudi Arabia
[4] Center for Advanced Material, King Fahd University of Petroleum and Minerals, Dhahran 31261, Saudi Arabia
[5] Interdisciplinary Research Center (RC) for Intelligent Secure Systems, KFUPM, Dhahran 31261, Saudi Arabia

[a)] **Author to whom correspondence should be addressed:** sens@iiti.ac.in

ABSTRACT

A new study explores the distinct roles of spontaneous polarization and piezoelectric polarization in piezo-phototronic coupling. This investigation focuses on differences in photocatalytic and piezo-photocatalytic performance using sodium bismuth titanate, a key ferroelectric material. The research aims to identify which type of polarization has a greater influence on piezo-phototronic effects. A theoretical assessment complements the experimental findings, providing additional insights. This study explores the enhanced piezo-phototronic performance of electrospun nanofibers compared to sol-gel particles under different illumination conditions (11 W UV, 250 W UV, and natural sunlight). Electrospun nanofibers exhibited a rate constant (k) improvement of 2.5 to 3.75 times, whereas sol-gel particles showed only 1.3 to 1.4 times higher performance when ultrasonication was added to photocatalysis. Analysis using first-principle methods revealed that nanofibers had an elastic modulus (C_{33}) about 2.15 times lower than sol-gel particles, indicating greater flexibility. The elongation of the lattice along the z axis in the case of nanofibers reduced the covalency in the Bi–O and Ti–O bonds. These structural differences reduced spontaneous polarization and piezoelectric stress coefficients (e_{31} and e_{33}). Despite having lower piezoelectric stress coefficients, higher flexibility in nanofibers led to a higher piezoelectric strain coefficient, 2.66 and 1.97 times greater than sol-gel particles, respectively. This improved the piezo-phototronic coupling for nanofibers.

INTRODUCTION

In contemporary devices, piezo-phototronic coupled properties are gaining importance. This is an interdisciplinary research field with a comprehensive aim of harnessing the tools of physics, chemistry, and nanotechnology. The field aims to study piezo-phototronic coupling in materials such as ferroelectrics. The piezo-phototronic coupling opens a three-way connection in piezoelectricity, semiconduction, and photonic properties in non-centrosymmetric materials.[1–3] By integrating piezoelectricity, photoexcitation, and semiconductor properties (piezo-phototronic coupling), one can introduce mechanical stimulation-induced polarization to generate a built-in electric field.[4,5] This development has spurred rapid progress in various fields, including transistors, nanogenerators, light-emitting diode (LEDs), and solar cells.[6] The piezo-potential can be used as a "gate" voltage to tune the charge recombination and modulate the performance of optoelectronic devices. However, an experimental result explaining the mechanism through theoretical assessment is necessary to understand such phenomena.

Such a piezo-phototronic effect is observed in non-centrosymmetric semiconductors. Several ferroelectric/piezoelectric simple oxides and perovskite oxides, such as ZnO, $SrTiO_3$, KNN, NBT, and $BaTiO_3$, are utilized in piezo-phototronic coupling.[7–11] One way to understand piezo-phototronic properties is to utilize piezo-photocatalytic activity, as it involves the photodegradation of organic dyes in the presence of external mechanical vibrations employing a piezoelectric effect. Nanomaterials such as nanoparticles and nanowires, with different surface morphology, have the capability of tuning the piezoelectric properties, enabling large bending compliance and flexibility, which allows efficient conversion of mechanical strain into charge carriers even at minimal strain levels.[12] Such a change in piezoelectric properties by changing the surface morphology can tune the piezo-photocatalytic activities.

The purpose of this work is not to understand the working of a device or understand the chemical potentials of a particular material in terms of photocatalysis but to uncover the underlying physics behind the piezo-phototronic coupling in a ferroelectric material such as sodium bismuth titanate (NBT). To justify the experimental work, a theoretical calculation is necessary. This requires understanding the subtle changes in the structure with which one can find the changes in the piezoelectric and spontaneous polarization. Hence, a detailed structural analysis of the material is required. To envisage the effect of spontaneous polarization, phonon studies are needed. A bandgap study needs to be presented to negate the reduction of the bandgap effect for the photocatalytic effect. The oxygen vacancy plays an important role in photocatalysis. Hence, such an effect must be elaborated for this subject. An oxidation state study is essential for this purpose.

Among various piezoelectric perovskite oxides, sodium bismuth titanate (NBT) ceramic is a potential material due to its high piezoelectric coefficient (d_{33}~70 pC/N), high remnant polarization (P_r~38 μC/cm^2), and chemical stability.[13–15] In addition, it possesses a high electrical conductivity (~10^{-5} S/m) among other perovskites, which is required for enhancement of the catalytic performance.[9] A work by Zhao *et al.* used hydrothermal synthesized NBT nanospheres to degrade RhB dye (k~0.061 min^{-1}) in the presence of a Xe-lamp.[9] Zhou *et al.* degraded various cationic dyes using the piezo-phototronic effect of NBT nanosphere (hydrothermal method) and nanorods (molten salt method) using a Xe-lamp, where nanorods (k~0.075 min^{-1} for MB) outperformed the nanospheres.[16] It was reported that nanorods possess a higher $d_{33}{}^*$~200 pm/V and simulated (Finite Element Method) piezopotential of −1.49 V than the nanospheres ($d_{33}{}^*$~100 pm/V, −0.27 V). A study by Liu *et al.* reported piezocatalytic degradation of MB dye (~54.2% in 150 min) using electrospun $0.93(Bi_{1/2}Na_{1/2})TiO_3–0.07BaTiO_3$ nanofibers.[17] Ji *et al.* utilized topochemical molten salt synthesis route grown thin sheets of NBT having strong ferroelectric polarization to study the photocatalytic performances.[18] A piezoelectric constant (d_{33}) of ~15 pm V^{-1} was reported by Ghasemian *et al.* for the hydrothermally grown NBT nanofibers.[19] In addition, considering only the piezo response of NBT nanostructures, oxygen vacancy also plays an important role in piezocatalytic activity.

A first principle-assisted study by Liu *et al.* reported that NBT with low O-vacancy exhibits robust piezoelectric properties.[20] This facilitates the generation of a large piezoelectric potential and accelerated charge transfer. However, the weak capacity to adsorb O_2 and OH^-, low electron concentration, and poor charge transfer and transport performance limit their piezocatalytic activity. Conversely, high O-vacancy demonstrates improved O_2 and OH^- adsorption capabilities, higher electron concentration, and enhanced charge transfer capacity. The accompanying reduction in d_{33} and weakening of the piezoelectric potential impair their photocatalytic performance, showcasing the double-edged sword role of O-vacancy in piezo-catalysis. Hence, the piezo-photocatalytic performance of NBT nanostructures significantly depends on the chosen preparation technology, which governs key factors, including morphology, size, oxygen vacancy, piezoelectric properties, and photoexcited response.

The reported work in the literature on nanostructured NBT emphasized tuning the piezo/photocatalytic performance based on modulating the morphology (specific surface area), conductivity, and piezoelectric coefficient. NBT has a high spontaneous polarization and piezoelectricity that depends on the crystal structure and the bonds participating in the structure having modifications in the electronic cloud distribution. A perspective on the impact of crystal structure and this electronic cloud distribution on spontaneous/piezoelectric polarization for different morphologies is missing in existing literature. This is one limitation in the field of piezo-phototronic coupling in ferroelectric materials. Hence, this work reveals, for the first time, the impact of crystal structure and lattice strain on the electronic clouds, consequently affecting the nanofibers' effective charge and polarization compared to bulk NBT. It uncovers how nanofibers elevate the piezo potential in the NBT unit cell. A clear distinction between ferroelectric spontaneous polarization and piezoelectric polarization needs special attention to understand which type of polarization exactly influences the piezo-phototronic coupling.[21,22] To study the differences between spontaneous and piezoelectric polarization, a novel investigation is being performed to find the differences between photocatalytic and piezo-photocatalytic performances of a prominent ferroelectric, as in NBT. A theoretical assessment is also performed to substantiate the findings. Two different samples with different morphologies are discussed to examine the importance of piezoelectric contribution.

$Na_{0.5}Bi_{0.5}TiO_3$ was synthesized using two different synthesis routes: sol-gel and electrospinning. These particles are referred to as sol-gel particles (SGP) and nanofibers (NF). Various characterization techniques such as XRD, Raman spectroscopy, scanning electron microscope (SEM)/transmission electron microscopy (TEM), diffuse reflectance spectroscopy (DRS), and x-ray photoelectron spectroscopy (XPS) were performed to distinguish the properties of SGP and NF. As extra information for the photocatalysis, two light sources (low-cost 11 W UV and high-cost 250 W UV lamps) were used to compare the cost efficiency of the process. In addition, natural sunlight was used to reduce the experimental cost further and show the utilization of NF as a catalyst. An attempt is made to understand the enhanced piezo-photocatalytic performance of the NF in terms of the structural parameters (c/a, tilt angle, and octahedral strain), phonon modes (Ti–O and TiO_6 vibrations), and piezoelectric coefficient (d_{33}). A theoretical approach is utilized to envisage the differences in the SGP and NF in terms of the lattice strain, electron localization, and the Born effective charges. Hence, a clear understanding of the improved flexibility, piezoelectric constant (d_{31} and d_{33}), and piezoelectric polarization of the NF compared to the SGP is thoroughly explained.

MATERIALS AND METHODS

Synthesis of SGP

All the precursors used for sol-gel and electrospinning were procured from Alfa–Aesar. For sol-gel synthesis, sodium nitrate (purity 99.9%) for Na and dihydroxy bis (ammonium lactate) titanium (IV) was dissolved in DI water in separate beakers, while bismuth nitrate pentahydrate (purity 98%) for Bi was dissolved in dilute nitric acid. The individual clear solutions were mixed and stirred until a completely homogeneous solution was formed. The gel was formed by adding citric acid and heating the solution at 80 °C. Furthermore, the gel was burnt using ethylene glycol, which was added to the solution (1:2 ratio of citric acid and ethylene glycol). The burnt powder was denitrified and decarburized at 450 °C for 12 h and 600 °C for 6 h. The phase formation was achieved at 700 °C for 10 h.

Synthesis of NF

For the electrospinning process, a clear solution was first prepared. Initially, sodium acetate was dissolved in equal amounts of acetic acid and methoxy ethanol, followed by the addition of Bi-nitrate to the solution to achieve a clear solution. An equal amount of acetylacetone was immediately added to the titanium precursor, Ti-isopropoxide (TTIP, 27.8%–28.6% TiO_2), in a separate beaker to stabilize the Ti precursor. Then, all the individual solutions were mixed in a single beaker to attain a clear solution. The solution was stirred continuously for 12 h. For the electrospinning process, a viscous solution was prepared by adding 10 ml methanol and 3 g of polyvinylpyrrolidone (PVP) to 10 ml of the prepared solution, followed by continuous stirring at room temperature for 12 h. Then, the solution was loaded into a syringe for the electrospinning to start. A collector voltage of 25 kV was applied by keeping a distance of 10 cm between the needle and drum collector (applied field 2.5 kV/cm) and keeping the feed rate at 1 ml/h. The drum collector speed was maintained to be 1000 rpm. A thick white mat-like sample was collected on the aluminum foil, which was further dried at 120 °C for 15 h to evaporate the solvents. Then, the samples were heated at 400 °C for 1 h and 700 °C for 1.5 h for phase formation.

Characterizations

The x-ray diffraction was performed on the prepared samples using Bruker D2-Phaser (Cu-K_α target) to check the structural information. Full-Prof Suite software was used for the Rietveld refinement of the obtained XRD pattern. The phonon modes were studied from Raman spectroscopy using a Horiba-made LabRAM HR Evolution Raman spectrometer (spectral resolution 1 cm^{-1}) having an He–Ne LASER of wavelength 633 nm. Fityk was used for the deconvolution of Raman spectra. Diffuse reflectance spectroscopy (DRS) study was performed in the range of 200–800 nm (UV–vis) using a Cary-60 Agilent UV–vis spectrophotometer to obtain the optical bandgap of the samples. The Supra55 Zeiss field emission scanning electron microscope (FE-SEM) was used to check the morphology. High-resolution transmission electron microscopy (HR-TEM) was performed using a TFS Talos 200FS system operated at 200 kV. Image J software was used to extract the SEM and TEM data information. X-ray photoelectron spectroscopy (XPS) data were obtained using a Kratos Axis Supra instrument equipped with a monochromatic Al Kα x-ray source ($h\nu$ = 1486.6 eV) operating at a power of 150 W and under UHV conditions in the range of ~10 × 10^{-9} mbar. All spectra were recorded in hybrid mode, using electrostatic and magnetic lenses and an aperture slot of 300 × 700 μm^2. The wide and high-resolution spectra were acquired at fixed analyzer pass energies of 80 and 20 eV, respectively. The samples were mounted in a floating mode to avoid differential charging, and thus, all spectra were acquired using charge neutralization. The XPS spectra were deconvoluted using XPSPEAK4.1 software. The spectra were calibrated using the C-1*s* peak (Binding energy = 284.8 eV). The background extraction was done using the Tougaard function. A combined Gaussian–Lorentzian peak shape was used for all the peaks to get quality fitting. Quanta chrome and the Autosorb iQ2 BET Surface Area and Pore Volume Analyzer measured specific surface area and pore volume.

Methylene blue (MB, $C_{16}H_{18}ClN_3S$, SRL chemicals, India) dye was used for the degradation process. A 5 ppm MB solution was prepared by adding 5 mg MB to 1 l DI water and stirring for 1 h. Then, 50 ml of this stock solution was taken in each beaker, and 62.5 mg of SGP and NF were added to respective beakers to prepare a concentration of 1.25 g/l. The prepared solution was stirred for 15 min. Then, the solution was kept undisturbed for 1 h to ensure proper solute and solvent adsorption–desorption equilibrium.

The photocatalysis experiment was performed using four low-pressure mercury-vapor (LPMV) discharge UV lamps, which emit UV radiation of wavelength ~253.7 nm (Philips TUV 11 W PLS) and a medium-pressure mercury vapor (MPMV) lamp of 250 W that emits UV radiation in the range of 200–600 nm. The piezo-photocatalysis was performed using the same light source and an ultrasonic vibration of 40 kHz with 200 W power using an ultrasonic cleanser. The intensity of 11 W light was ~700lx (5.53 W/m^2) and 250 W light was ~5000 lx (39.5 W/m^2), which is ~181 and ~25.3 times lesser than the AM 1.5 G sun (1000.4 W/m^2), respectively. A similar piezo-photo coupling experiment was performed for the nanofibers under natural sunlight having a surrounding temperature of ~30–35 °C (~70 000 lx~1.56 times lesser than the AM 1.5 G sun ~109 880 lx). While experimenting, the solution was kept in a water bath to ensure the temperature does not reach beyond 35 °C. The light and sonication were given for 15 min, and then, the solution was kept to rest under dark conditions for another 10 min. Then, 5 ml solution was transferred to a centrifuge tube and centrifuged for 15 min at an rpm of 5000. The centrifuged solution was further used to record the absorbance using the UV–vis setup by ResearchGate India.

Computational details

Spin-polarized density functional theory calculations were performed using the Vienna *Ab Initio* Simulation Package (VASP). The plane-augmented wave (PAW) method is used for the electron–ion interactions. The PBE functionals within the GGA approximations were used to treat the exchange–correlation part better. A cutoff of 500 eV is used for the representation of Kohn–Sham wavefunctions, and a conjugate-gradient algorithm is used for structural relaxation and optimization. An energy convergence criterion is set to 10^{-6} eV. All the geometric structures are optimized until the Hellmann–Feynman forces on each atom are reduced to 0.01 eV/angs. A Γ-centered **k** point grid of 11 × 11 × 4 is used to sample the Brillouin zone (BZ) for the NBT unit cell. To account for the exact electron correlation, the (Heyd–Scuseria–Ernzerhof) HSE06 and metaGGA (SCAN) functionals are employed to accurately describe electronic properties.

Some *ab initio* simulations were carried out using the VASP code to calculate the piezoelectric stress coefficient, ${e_{ijk}}^{T}$, from density functional perturbation theory (DFPT). For the calculation of mechanical [elastic tensor; C_{ij}, compliance tensor; s_{ij} $(=C_{ij}^{-1} \times I)$ and piezoelectric properties (piezoelectric tensor; e_{ijk}^{T}, Born effective charges; Z_{ij}^{*}) with ionic contributions, an energy cutoff of 1000 eV was used for an accurate description of the Hessian matrix.

RESULTS AND DISCUSSION

The x-ray diffraction pattern revealed the presence of a single phase in both the SGP and NF samples. The broadening of the XRD pattern for the NFs revealed a smaller particle size than the SGP [Fig. 1(a)]. The Rietveld refinement confirms that the samples are in the rhombohedral ($R3c$) phase [Figs. S1(a)–S1(b)]. The lattice parameters $a = b$ and c for NF [5.5146(24), 13.5059(32) Å] showed a higher value than the SGP [5.5066(20), 13.4574(9) Å] sample. The c/a ratio represents the lattice distortion along the c axis, which influences the piezoelectric properties of a material. A higher c/a and rhombohedral lattice distortion ($\eta_R = \frac{c}{\sqrt{6}a} - 1$) was observed for the NF (Table I). Octahedral tilt ($\omega = 4 \times \sqrt{3} \times e$) is an important parameter to understand ferroelectric perovskites that are derived from the atomic positions using the Megaw Darlington approach.[23] The tilt angle is higher for the NF (5.26°) than the SGP (4.06°) sample [Fig. 1(c)]. "ζ" is the octahedral strain, given by $\zeta = \cos(\omega)\left(\frac{C_H}{\sqrt{6}a_H}\right) - 1$. The parameter 1 + ζ indicates the elongation and flattening of the octahedra along the triad axis. 1 + ζ is also higher for the NF (0.995 67) than the SGP (0.995 21). The distinct difference between NF and SGP is their preferred arrangement of particles in a certain manner specific to their respective

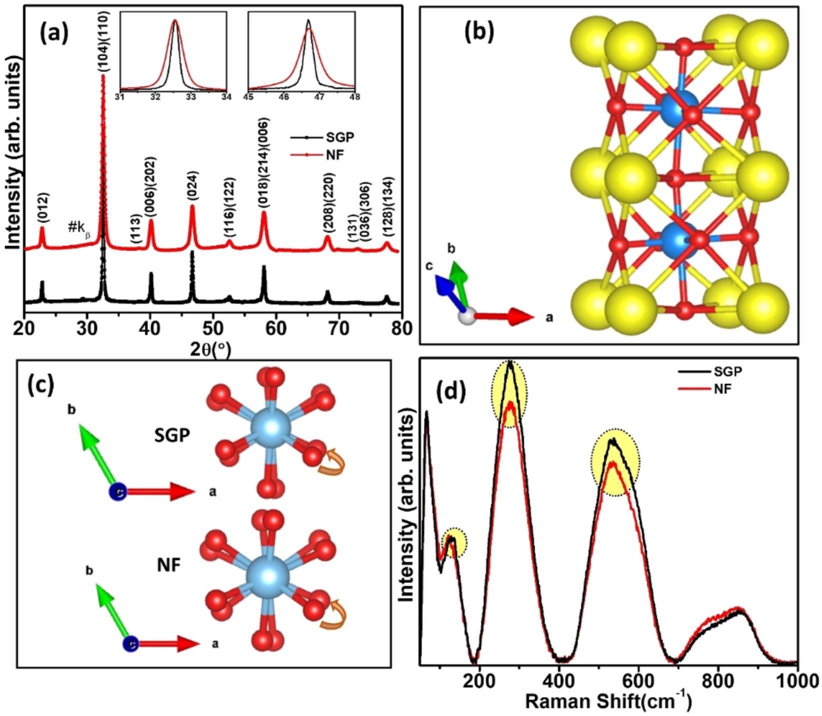

FIG. 1. (a) X-ray diffraction pattern for sol-gel prepared NBT (SGP) and electrospun nanofiber (NF), (b) perovskite structure diagram for electrospun nanofiber (NF), (c) tilt angle of alternate TiO_6 octahedra for sol-gel prepared NBT (SGP) and electrospun nanofiber (NF), and (d) Raman spectra for sol-gel prepared (SGP) and electrospun nanofiber (NF). [Yellow atoms → A-site occupying atoms (Na/Bi), blue atoms → Ti, and red atoms → O].

TABLE I. Tabulation of the lattice parameters, volume, *c/a*, rhombohedral distortion, tilt angle, and octahedral distortion parameters derived from the CIF file after Rietveld refinement of the sol-gel prepared (SGP) and electrospun nanofiber (NF) NBT.

	Lattice parameters						
Sample	$a = b$ (Å)	c (Å)	c/a	Volume (V) (Å^3)	Rhombohedral distortion (η_R)	Tilt angle (ω)	Octahedral distortion (1 + ς)
SGP	5.5066(92)	13.4574(9)	2.4438	353.40(3)	−0.0023	4.06°	0.9952
NF	5.5146(24)	13.5059(3)	2.4491	355.70(3)	−0.0001	5.26°	0.9957

synthesis conditions. The SGP preferred accumulating the particles spherically, leaving no preferred growth direction. However, the NF arranged the particles in a chain, showing a preferred growth direction due to the particle confinement in the other two directions. Such preferential nucleation and growth affected the lattice strain, leading to the lattice's elongation along the c axis and thereby enhancing the *c*/*a* ratio for the NF compared to the SGP. This ultimately generated a higher octahedral strain in the NF.

A higher *c*/*a* and octahedral strain generates more distortion, which enhances the piezoelectric performance in NBT-based materials.[13] Hence, based on structural analysis, it can be inferred that the nanofibers can be an advantage for piezoelectric applications compared to the SGP samples.

According to group theory, rhombohedral (*R*3c) NBT should possess 13 Raman active modes ($\Gamma_{R3c} = 4A_1 + 9E$). The crystallographic sites 6(a) (Na/Bi/Ti positions) correspond to four Raman ($A_1 + 2E$), whereas crystallographic sites 18(b) (O-atom position) in hexagonal settings correspond to nine Raman ($3A_1 + 6E$) active modes.[24] However, the experimental Raman spectra for NFs, in the range of 50–1000 cm^{-1}, revealed only seven major modes at 66 cm^{-1} (A_1), 122 cm^{-1} (E), 279 cm^{-1} (A_1), 531 cm^{-1} (E), 604 cm^{-1} (E), 774 cm^{-1} (A_1), and 857 cm^{-1} [Fig. S1(c)]. The Raman shifts for the SGP were observed to be at 66 cm^{-1} (A_1), 128 cm^{-1} (E), 279 cm^{-1} (A_1), 531 cm^{-1} (E), 604 cm^{-1} (E), 774 cm^{-1} (A_1), and 857 cm^{-1} [Fig. S1(d)]. The FWHM of the NF and SGP were found to be similar. The intensity of the NF was reduced compared to the SGP sample [Fig. 1(d)]. The changes in the Raman spectra can be attributed to the variations in the synthesis route. These affect the particle size and strain. The local structural changes and the associated strain affect the phonons, which can be detected using Raman spectroscopy.

"E" mode for NF was observed at 122 cm^{-1}, while for the SGP, it was 128 cm^{-1}. The A–O bond length was observed to increase from 2.757 76 (5) Å (SGP) to 2.761 67 (5) Å (NF). This hints at a decrease in the bond strength, which may be the reason for the redshift. However, the changes in the Raman shift were negligible for the other modes.

A prominent observation was the change in the intensity ratio of the A_1 mode at 66 cm^{-1} to the A_1 mode at 279 cm^{-1} for the NF and SGP. The ratio was found to be 1.13 for NF and 1.25 for SGP. Similarly, the intensity ratio of the A_1 (66 cm^{-1}) mode to the E mode at 531 cm^{-1} also showed a difference between the NF (0.84) and the SGP (0.90). Hence, these intensity ratios decreased for both cases, as in the case of NF [Fig. 1(d)].

For the NFs, the FWHM changes significantly for two modes. The E mode (~604 cm^{-1}, TiO_6 octahedral vibration) showed an increase in FWHM from ~68 cm^{-1} (NF) to 70 cm^{-1} (SGP). On the other hand, the FWHM of the A_1 breathing mode (~774 cm^{-1}) decreased from ~94 cm^{-1} (NF) to 92 cm^{-1} (SGP). The broadening of the E mode could be associated with the strain induced in the lattice, which is also responsible for the reduction of the crystallite size of the NF. On the other hand, the nominal sharpening of the breathing A_1 mode can be due to a decrease in octahedral tilt (ω) in SGP compared to the NF.

The FESEM studies enabled the understanding of the formation of the nanocrystallites in the SGP and the NF case. The morphology of the SGP samples revealed agglomerated particles (~2.068 μm) of almost spherical morphology [Figs. 2(a) and 2(b)]. However, these particles appear to be constituted of sub-100 nm nanocrystallites. On the other hand, the electro-spun sample showed elongated tubular nanofibers of length 4–5 μm and with diameters of ~273 nm [Fig. 2(d)]. However, these nanofibers also seem to comprise sub-100 nm nanocrystallites. The average nano-crystallite size of the SGP sample appeared larger than the NF. It should be noted that the tubular nanofibers were derived from as-deposited fibers of a diameter of ~894 nm, which were further annealed at 700 °C to obtain the final phase-formed nanofiber of a smaller diameter of ~273 nm. The heating at 700 °C also shortened the length of the

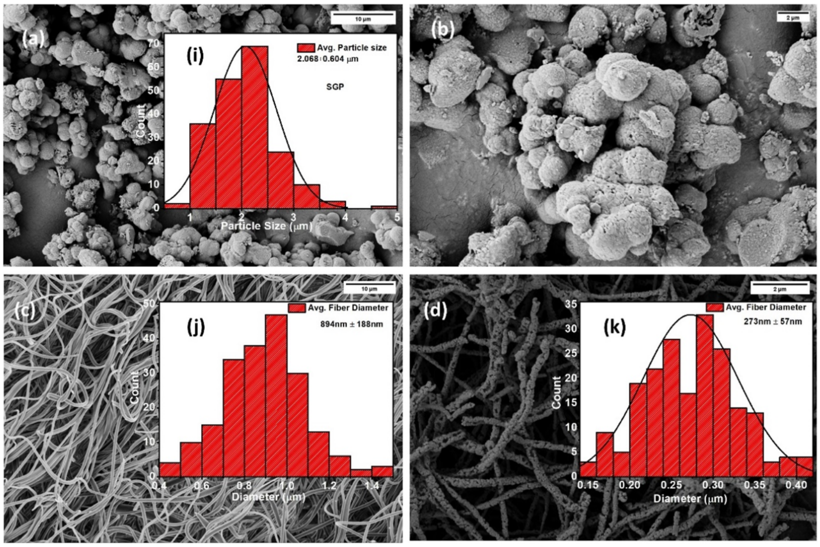

FIG. 2. FESEM images of (a) sol-gel prepared SGP NBT, (b) sol-gel prepared SGP NBT showing agglomerated spherical morphology, (c) electrospun NBT nanofibers (NF) after drying at 120 °C, and (d) electrospun NBT nanofibers (NF) annealed at 700 °C. [(i) particle size distribution of agglomerated microspheres of sol-gel NBT (SGP), (j) nanofiber diameter distribution of 120 °C dried electrospun NBT (NF), and (k) nanofiber diameter distribution of 700 °C annealed and phase formed electrospun NBT (NF)].

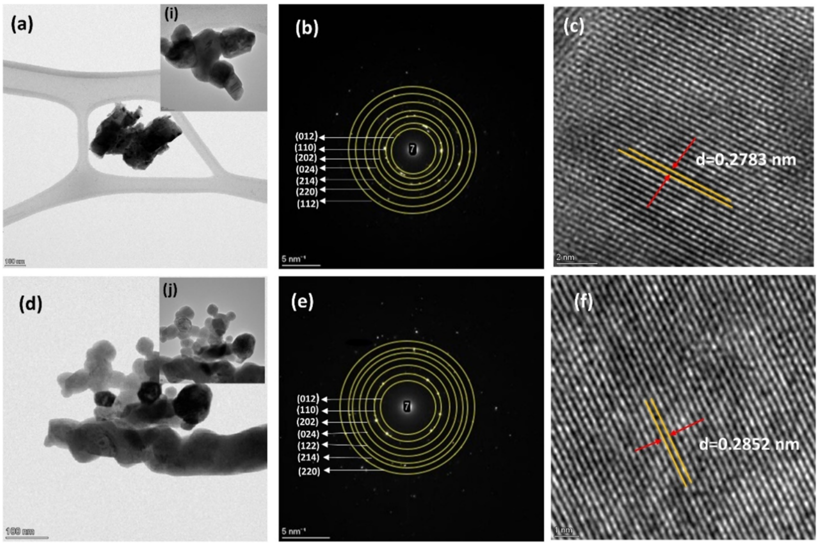

FIG. 3. (a) TEM image of sol-gel prepared NBT (SGP), (b) SAED pattern of SGP confirming *R*3c phase, (c) HRTEM image of SGP showing d-spacing for (110) plane, (d) TEM image of electrospun NBT nanofiber (NF), (e) SAED pattern of NF confirming *R*3c phase, and (f) HRTEM image of NF showing *d*-spacing for (110) plane. [TEM image of NBT at 50 nm scale: (i) sol-gel prepared SGP and (j) electrospun NBT nanofiber (NF)].

fiber from several micrometers to a few micrometres [Fig. 2(c)]. It should be noted that the as-deposited fibers appeared to be a continuous thread-like structure that became an array of nanoparticles upon heating due to surface/grain boundary diffusion and local evaporation-condensation processes.[25]

Transmission electron microscopy (TEM) was performed to understand the structure and nano-crystallite morphology. Both samples revealed nano-sized particles of size ~70 nm for SGP and ~40 nm for NF [Figs. 3(a) and 3(d)]. Selected area electron diffraction (SAED) images revealed at least one circle of several bright spots. However, one can analyze the TEM results to be constituted of complex diffraction patterns from individual crystallites in different orientations, resulting in as many as seven concentric rings [Figs. 3(b) and 3(e)]. The d-spacing obtained from these concentric circles matches with the *d*-spacings of the XRD results. High-resolution transmission electron microscopy (HRTEM) unveiled nuanced phase contrast images, illuminating distinctive grain orientations corresponding to (110) and (012) crystal planes, delineated by d-spacing dimensions of 0.27 and 0.35 nm, respectively [Figs. 3(c), 3(f), S2, and S3]. Moreover, elemental analysis elucidated the presence of only sodium (Na), bismuth (Bi), titanium (Ti), and oxygen (O) constituents within both the SGP and NF, thereby ensuring the phase purity of the materials (Fig. S4).

The N_2 adsorption–desorption curve obtained from the BET measurement revealed a higher specific surface area of ~10.573 m^2/g for the NF calculated from the adsorption curve (Fig. S6). The pore volume and the average pore diameter were found to be 0.075 cc/g and 17.58 Å, respectively. The SGP sample did not reveal consistent results, which may be due to the less porous structure.

The modified Kubelka–Munk equation is given by the relation, $F(R_\infty) \propto \frac{(h\nu - E_g)^{\frac{1}{n}}}{h\nu}$, $(F(R_\infty)h\nu)^n = A(h\nu - E_g)$ used to calculate the bandgap of SGP and NF.[26,27] For the direct bandgap transition, "*n*" is considered to be 2, and for the indirect transition, ½ is used. A plot between $[F(R)\ h\nu]\ n$ vs "energy ($h\nu$)," known as the Tauc plot, was used. It generated a straight line with an x-axis intercept equivalent to the bandgap (E_g) for direct and indirect cases. In the literature, NBT-based samples have been reported to have both direct and indirect bandgaps.[28] In this case, NF revealed a higher direct bandgap (E_{gd} = 3.34 eV) than the indirect bandgap (E_{gi} = 3.25 eV) [Figs. 4(a) and 4(b)]. Similarly, for the SGP samples, E_{gd} was found to be 3.17 eV while E_{gi} was 3.08 eV. It should be noted that both

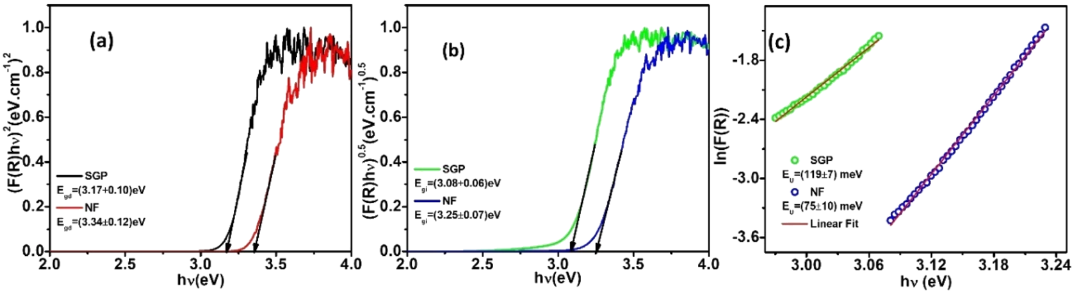

FIG. 4. (a) Direct bandgap, (b) indirect bandgap, and (c) Urbach energy for SGP and NF.

values are lesser for the SGP than the NF. A theoretical calculation is essential to understand this behavior, which will be discussed in the following section.

Disorders and strain in the lattice can result in tailing states near the band edges, resulting in an exponential increase in $F(R)$, with energy ($h\nu$). These tailing states are known as the Urbach tail and can be related to the Urbach energy (E_U) as $F(R) = (F(R))_0 \exp\left(\frac{h\nu - E_g}{E_U}\right)$, where $F(R)_0$ is a material constant.[29] The above can be modified by taking logarithms on both sides and being written as $\ln(F(R)) = \ln(F(R))_0 + \frac{h\nu - E_g}{E_U}$. Hence, the inverse of the slope obtained from linear fitting of the plot between $\ln[F(R)]$ vs "$h\nu$" gives E_U. Urbach energy was observed to be lesser for the NF (75 meV) in comparison with the SGP (119 meV) [Fig. 4(c)]. As the Urbach tail is due to the disorder in the lattice, the changes in the defects in the samples affect the Urbach energy. The O_v creates an intermediate state near the conduction band within the bandgap.[20] This introduces the bandgap tailing near the absorption energy. The decrease in the Urbach energy for the NF compared to the SGP indicated a decrease in defects in the NF. From the XPS analysis, it was observed that the oxygen vacancy (O_v) is lesser for the NF (~16%) compared to the SGP (~26%) (Fig. S5). Such a decrease in the O_v for the NF is possibly due to the requirement of a much lesser annealing time (1.5 h) compared to the SGP (10 h) to synthesize the single-phase NBT samples.

The spin-polarized density functional calculations using VASP revealed the theoretical electronic structure of the ideal NBT-SGP structure at its equilibrium volume. Employing GGA approximations, a bandgap of 2.47 eV was calculated, which was noticeably lower than the experimentally observed indirect bandgap of 3.08 eV. This discrepancy underscores the inherent limitations of GGA methods in accurately describing the electronic structure. This is likely due to the lack of exact electronic correlations. A single DFT functional that can perfectly describe the electronic structure of materials is impossible. Hence, more DFT functionals, such as Hybrid (HSE06) and metaGGA (SCAN), were considered. A k-resolved DOS is plotted along the high-symmetry BZ path for all three approximations (Fig. 5) to understand the hybridization within the vicinity of the electronic gap. The calculated bandgaps using the HSE06 (3.64 eV) and SCAN (2.76 eV) functionals are shown in Figs. 5(a) and 5(b).

Among the three approximations, the SCAN DFT functional is in much closer agreement with experimental observations. The conduction band minima (CBM) lie at the Γ-point, and the valence band maxima (VBM) lies between the T-H2. A k-resolved DOS is plotted along the high-symmetry BZ path for each element (Fig. 6) to understand the hybridization within the vicinity of the electronic gap. The Ti-states majorly contribute to the CBM, with some partial occupation of Bi and O states. In the case of VBM, it is mainly occupied by the O states with some partial Bi occupation. The Fermi level is observed to be close to the valence band, i.e., the O states. Na-states are highly stabilized at the Fermi level.

An internal strain is generated with the evolution of the particle's size and shape. This strain significantly modifies the lattice structure and thereby modifies the electronic structure. Several scenarios of lattice strain were considered, e.g., isotropic, lateral, and uniaxial strain, keeping the volumetric strain constant for each case. Considering these potential scenarios, the electronic gap's nature in NBT nanofibers was simulated using SCAN DFT functionals. The calculated bandgaps are 2.82 eV (expansion) and 2.57 eV (compression) for isotropic strain. Similarly, for lateral strain, these values were 2.68 eV (expansion) and 2.55 eV (compression), while for uniaxial strain, the values were 2.99 eV (expansion) and 2.03 eV (compression) (Fig. S7). The difference between the SGP and NF bandgaps can be observed experimentally to be ~0.17 eV for both direct and indirect bandgaps. Theoretically, all the calculations show an indirect bandgap. The indirect E_g from the SCAN calculations was 2.76 eV for the NBT SGP sample. The differences of this E_{gi} were calculated with all the six possible cases of a strained NBT lattice. From these differences, the uniaxial expansion revealed a difference of ~0.23 eV. Hence, uniaxial expansion appears to be the most feasible strain scenario in these nanofibers (NF). Following the observations on the electronic structure and experimental observations, only the DFT-optimized equilibrium and uniaxial expansion structure were considered for further analysis of piezoelectric properties.

Photocatalysis/piezo-phototronics effect

This work has investigated a simple process to understand the effect on the piezoelectric properties in the presence of light in terms of understanding the changes in the photodegradation process in the

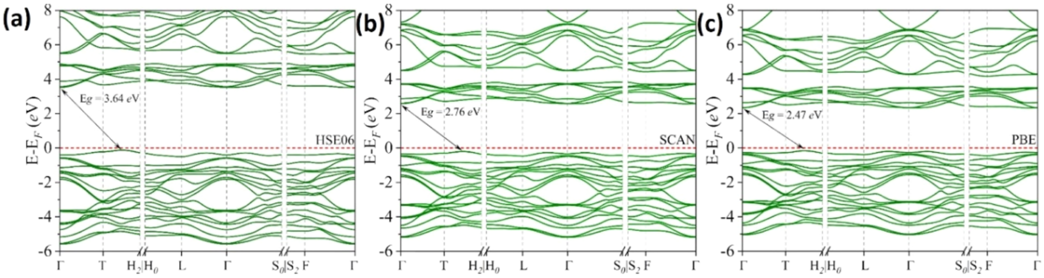

FIG. 5. Band-structure of NBT (SGP) calculated using (a) HSE06, (b) SCAN, and (c) PBE-DFT functionals. The Fermi level is set to 0 eV, keeping the equilibrium geometry fixed, obtained from GGA-PBE functionals.

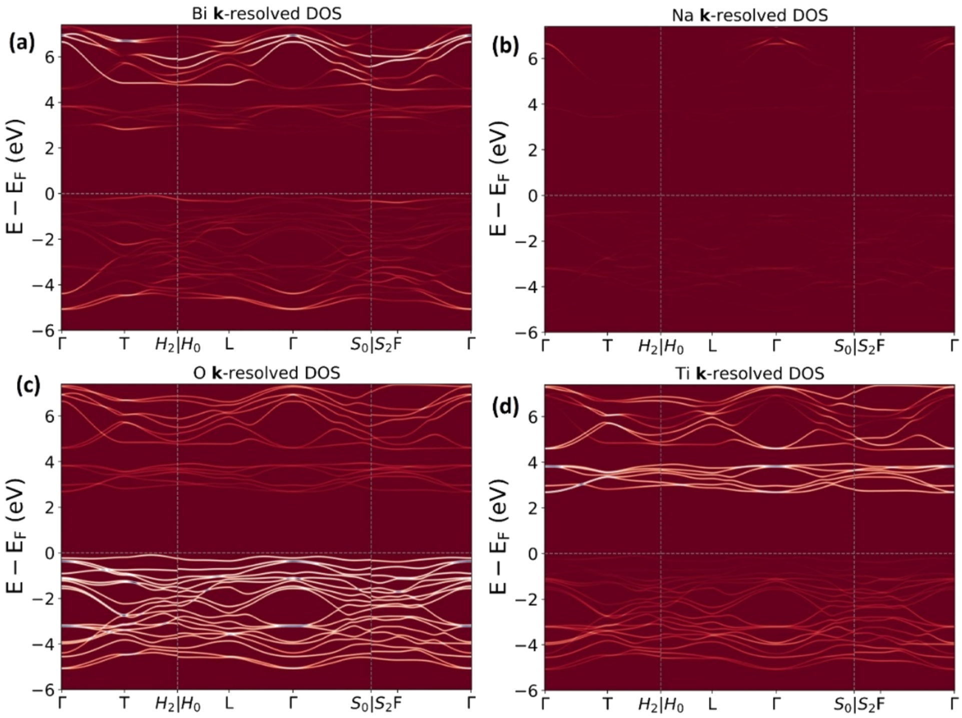

FIG. 6. Atom-resolved k-resolved (DOS) projected along the high-symmetry lines calculated using the SCAN DFT functionals for (a) Bi-atom, (b) Na-atom, (c) O-atom, and (d) Ti-atom. (The conduction band is majorly populated with Ti-states, whereas the valence band is with O-states).

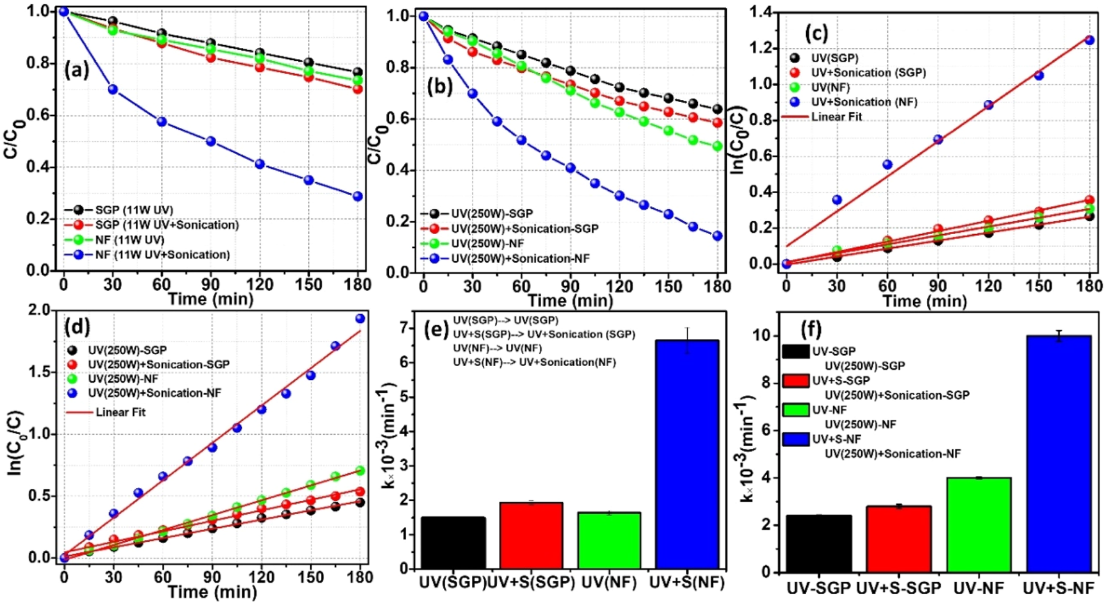

FIG. 7. Relative concentration change of MB dye with an increase in photon irradiation time for SGP and nanofiber under two conditions: (a) 11 W UV and (b) 250 W UV; rate of change of MB dye concentration with time for both SGP and nanofiber under two conditions: (c) 11 W UV and (d) 250 W UV; and comparison of rate constant "*k*" for SGP and nanofiber for only photocatalysis and piezo-photocatalysis under two conditions; (e) 11 W UV and (f) 250 W UV.

presence of light and external mechanical vibrations. As a source of mechanical vibrations, an ultrasonication process has been adopted. The degradation of methylene blue (MB) dye (5 ppm) was investigated in the presence of a 40 kHz ultrasonic bath while irradiating with photons of two different types of artificial sources: (1) LPMV 11 W UV light and (2) MPMV 250 W UV light.

Four different concentrations of NF were experimented with: 0.5, 1, 1.25, and 1.5 g/l. The degradation increased with the NF concentration from 65% (0.5 g/l) to 68% (1 g/l) and a maximum of ~71% for 1.25 g/l under UV (11 W) (Fig. S8). Further increasing the concentration reduced the degradation rate. Increasing the catalyst amount in heterogeneous photocatalysis leads to intensified photodegradation due to elevated collisions between reactants and increased formation of OH· radicals on the photocatalyst surface. However, beyond a threshold catalyst quantity, turbidity in the solution impedes the reaction by obstructing the necessary radiation, resulting in a decline in degradation percentage.[30] Hence, a 1.25 g/l concentration was selected to further investigate the piezo-photo coupling in SGP and NF samples.

A similar study was performed without the vibrations on the 1.25 g/l SGP and nanofiber samples to understand the effect of the ultrasonic vibrations. The time-resolved absorbance spectra are shown in Fig. S8. With time, there was a steady decrease in MB concentrations. The degradation efficiencies in percentage were determined using the equation, $Degradation\% = \left(\frac{C-C_0}{C_0}\right) \times 100$. Degradation was observed for all the concentrations of both samples, revealing a universality of the catalytic activity of the NBT samples. However, NF degraded the MB solution at a higher rate for all irradiation types and intensities than the SGP (Fig. 7). The degradation for nanofibers was ~30% after 180 min illumination of the 11 W UV light, while for SGP, it was ~23%. For the 250 W illumination, the degradation after 180 min was ~41% for the nanofiber and ~36% for the SGP sample (Table II). The degradation increase under higher power illumination may be due to the available number of photons in the 250 W source. However, considering the bandgap to be ~3.08 eV, such utilization of lesser energy light is less probable until one considers defect states in the samples. However, one must also consider that intensity dependence is not a straightforward correlation, considering the difference in powers of the two light sources. This aspect thus instigates a further detailed intensity-dependent study of the two individual sources of the degradation mechanism. However, the scope of this work is to focus on the effect of sonication on the photodegradation process. Both nanofibers and SGP showed enhanced degradation under the simultaneous influence of light and ultrasonic vibration. The degradation for the NF samples was observed to be ~71% with the 11 W and ~85% with 250 W light illumination for 180 min. The SGP revealed a much lesser degradation of ~26% for 11 W and ~50% for 250 W for the same illumination time, i.e., 180 min (Table II). Hence, the NF exhibit better photocatalytic activity than the SGP counterpart with and without the involvement of sonication. This could be related to the high specific surface area of NF.

Photocatalysis in semiconductors generally comprises three underlying steps:[31,32]

1. Photon absorption and generation of electron–hole pairs: light irradiation on the photocatalyst promotes the transfer of electrons from the valence band to the conduction band, leaving holes in the valence band and thereby creating electron–hole pairs.
2. Separation of excited charges and migration to the surface from lattice: electron–hole pairs generated by light absorption are separated before they recombine. This separation is crucial for achieving efficient catalytic reactions because it allows the charges to participate in redox reactions at different sites of the photocatalyst material.
3. Involvement of the electrons and holes in the redox reactions at the surfaces.

The performance of any photocatalysts mostly depends upon the charge separation and transfer kinetics. During the

TABLE II. Degradation percentage (%) and the rate constant (k) for different irradiation and vibration conditions for sol-gel particle (SGP) and nanofiber (NF). [L→ only light and L + S→ light + sonication].

Degradation percentages and rate constants		Samples	
		SGP	NF
Degradation in 180 min (%) (11 W)	L	23	26
	L + S	30	71
Degradation in 180 min (%) (250 W)	L	36	51
	L + S	41	85
Degradation in 180 min (%) (natural sunlight)	L	25	60
	L + S	32	75
Rate constant (k) in min^{-1} ($\times 10^{-}3$) (11 W)	L	1.48 ± 0.02	1.64 ± 0.06
	L + S	1.93 ± 0.05	6.65 ± 0.40
Rate constant (k) in min^{-1} ($\times 10-3$) (250 W)	L	2.48 ± 0.04	4.00 ± 0.05
	L + S	2.83 ± 0.09	10.06 ± 0.24
Rate constant (k) in min^{-1} ($\times 10-3$) (natural sunlight)	L	4.78 ± 0.08	14.97 ± 0.14
	L + S	6.41 ± 0.06	23.20 ± 0.72

photocatalysis, most electron–hole pairs undergo recombination, either during transit to the surface or upon reaching surface sites.[33–35] This recombination process results in the dissipation of harvested energy in nonradiative heat dissipation (capture) or radiative recombination (light). Such capturing or recombination of the photoinduced carriers in the lattice or surface significantly reduces the photocatalytic performance.

A piezoelectric material has a built-in dipole due to the application of an external field or strain, which gives rise to dipole polarization. The interaction between piezoelectric polarization and electronic transport leads to advantageous synergistic outcomes. Applying external strain to a piezoelectric material lets one control charge transport, recombination, or separation of the charge centers. Hence, such an external strain-induced polarization in piezoelectric materials facilitates the process of manipulation of charge-carrier transport properties within the lattice.[36,37] The movement of photoinduced charges, i.e., electrons/holes, can be manipulated, restricting recombination by enhancing their physical separation. In the present study, the ultrasonic vibration generated the required mechanical vibrations that facilitate the physical separation of the electron–hole pairs. From the experimental results, the NFs are observed to be more sensitive to mechanical vibrations than the SGPs. This may be due to the morphology of the nanofibers, which can be more sensitive to the vibrations and thereby result in higher built-in polarization.[16]

The kinetics of the dye degradation process can be expressed using the relation: $C = C_0 e^{-kt}$, where "C" is the concentration at time t, "C_0" is the initial concentration at $t = 0$, and "k" is the first order rate constant. In addition, "k" was calculated from the linear fitting of $\ln(C_0/C)$ and time (t) [Figs. 7(c) and 7(d)] for both the samples. The linear fitting details are presented in Table SII. The "k" value obtained for the photocatalytic effect in irradiated nanofiber was 0.0016 min^{-1} (11 W) and 0.004 min^{-1} (250 W), while for the irradiated SGP sample was 0.0014 min^{-1} (11 W) and 0.002 min^{-1} (250 W). Hence, the NBT nanofibers showed a higher "k" than the SGP sample. A higher "k" represents a better catalytic performance.

Similarly, for the piezo-phototronic effect, the "k" value obtained for the NF was 0.006 min^{-1} (11 W) and 0.010 min^{-1} (250 W), while for the SGP, it was 0.0019 min^{-1} (11 W) and 0.0028 min^{-1} (250 W). Hence, it is observed that the "k" value has increased from 0.0016 to 0.006 min^{-1} for the 11 W illumination with the application of sonication (Table II). This increases 3.75 times, establishing a strong piezo-phototronic effect in the NF for 11 W illumination. Similarly, for the 250 W illumination, NF exhibited 2.5 times enhancement for the sonication. These are noteworthy, remarkable improvements in the piezo-phototronic catalytic performance of NBT nanofibers. Similarly, for the SGP samples, the piezo-phototronic improvement was 1.35(11 W) and 1.40 (250 W) times. Hence, NF exhibits better improvement with the application of ultrasonic vibration than the SGP. One important information extracted from this study is the ability to achieve better performance of nanofibers even under low power (11 W) illumination. This is a significant contribution to reducing costs in functionality performance.

The nanofibers were stable even after the piezo-phototronic effect (Fig. S20). The XRD patterns of the recovered nanofibers after the piezo-phototronic coupling under 11 and 250 W irradiation conditions were recorded. Rietveld refinement was performed to understand the structural changes (Fig. S21). The rhombohedral ($R3c$) phase was retained after the piezo-photocatalysis experiment, revealing structural stability. The nominal changes in structural parameters are small enough to be reported (see the supplementary material for details). After the piezo-photocatalysis under 250 W UV and sonication, the recovered nanofibers were reused for up to three consecutive cycles (Fig. S23). The degradation % obtained for the three cycles was observed to be ~89% for the first cycle, ~81% for the second cycle, and ~85% for the third cycle. This value is within the range mentioned for the initial untreated nanofiber piezo-photocatalyst (~85%). The error percentage of this measurement is within ~5%, emphasizing the sustainability of the photocatalytic properties upon repeated use.

One more experiment was performed to reduce the cost of the experiment using natural sunlight. A similar comparison was performed on both samples with natural sunlight illumination for 60 min (Fig. S12). The "k" values for the nanofibers were 0.015 min^{-1} (photocatalysis) and 0.023 min^{-1} (piezo-photocatalysis). This is an improvement of 1.53 times using the ultrasonic vibration, revealing a strong piezo-phototronic coupling in the nanofibers. On the other hand, the "k" values for the SGP sample were 0.004 min^{-1} (photocatalysis) and 0.006 min^{-1} (piezo-photocatalysis). This is an improvement of 1.50 times using the ultrasonic vibration, revealing a similar strong piezo-phototronic coupling in the SGP. This reveals a universal improvement of any illumination due to piezo-phototronic coupling in the nanofibers and SGP. It should be noted that the "k" values of the SGP are quite lower than those of the nanofibers in the case of natural sunlight. Hence, piezo-phototronic catalysis in natural sunlight using nanofibers can be a prominent process of successful dye degradation in the daytime.

Ab initio simulation

The induced polarization (along i, P_i) by a unit displacement (along j, u_j) of the sublattice of atoms gives rise to Born effective charge tensor ($Z^*{}_{ij}$): $Z^*_{ij} = \frac{\partial P_i}{\partial u_j}$.[38] The off-centering of ions responsible for the ferroelectric effect can be understood by the Born effective charges.[39,40] The Born effective charges components along the diagonal ($Z^*{}_{xx}$, $Z^*{}_{yy}$, $Z^*{}_{zz}$) and off-diagonal (Z_{xy}, Z_{yx}) of the charge tensor for Na, Bi, Ti, and O atoms are presented in Table SIII. As Na, Bi, and Ti atoms possess high local site symmetry, their effective charge tensors give rise to almost diagonal tensors with two independent components showing less anisotropy ($Z^*{}_{xx} = Z^*{}_{yy}$, $Z^*{}_{zz}$). Due to less symmetry in the O atoms, the effective charge tensor is more anisotropic, having all the independent components. It can be observed that the effective charges of Bi, Ti, and O atoms showed a significant deviation from the ideal ionic values (+3: Bi, +4: Ti, and −2: O). This represents the mixed ionic and covalent bonding in Bi–O and Ti–O due to the hybridization of Bi-6p and Ti-3d orbitals with the O-2p orbitals for both SGP and NF.[41]

One independent component in the Born-effective diagonal tensor can be observed for the Na atom. However, a small off-diagonal antisymmetric component ($Z^*{}_{xy} = -Z^*{}_{yx}$) was observed for both SGP (0.047) and NF (0.054). This indicates that the Na atom is comparatively isotropic than other atoms. The effective charge density ($Z^*{}_{xx} = Z^*{}_{yy}$, $Z^*{}_{zz}$) values for both SGP (1.112, 1.126) and

NF (1.140, 1.195) are close to the ideal ionic value i.e., +1. This was observed for both SGP and NF. The effective charges were observed to be nominally higher for the NF.

For the Bi-atom, two independent components were observed along the diagonal, one parallel to the z axis (Z^*_{zz}) and the other two perpendicular to the z axis ($Z^*_{xx} = Z^*_{yy}$). The $Z^*_{xx} = Z^*_{yy}$ components are +5.364 for the SGP and +5.246 for the NF. Similarly, Z^*_{zz} values are +3.772 for the SGP and +3.171 for the NF. These values are also higher than the ideal ionic value (+3). In addition, it should be noted that the nanofibers exhibited a lesser effective charge than the SGP for all the diagonal components. An off-diagonal component $Z^*_{xy} = -Z^*_{xy}$ was observed for SGP (−0.651) and NF (−0.735). This makes Bi comparatively anisotropic than Na atom.

Two independent components were also observed for the Ti1-atom (0, 0, z). The $Z^*_{xx} = Z^*_{yy}$ components are +6.173 for the SGP and +5.243 for the NF. Similarly, Z^*_{zz} values are +6.099 for the SGP and +4.614 for the NF. These values are significantly higher than the ideal ionic value of +4. It can be observed that the NF exhibited a significantly lesser effective charge than the SGP for the Ti1 atom.

For the Ti2-atom (1/3, 2/3, z), two independent components were observed along the diagonal of the tensor, one parallel to the z axis (Z^*_{zz}) and the other two perpendicular to the z axis ($Z^*_{xx} = Z^*_{yy}$). The $Z^*_{xx} = Z^*_{yy}$ components are +7.403 for the SGP and +6.812 for the NF. Similarly, Z^*_{zz} values are +6.099 for the SGP and +4.614 for the NF. These values are significantly higher than the ideal ionic value of +4. It can be observed that the nanofibers exhibited quite a lesser effective charge than the SGP for all the diagonal components for the Ti2 atom. An off-diagonal component $Z^*_{xy} = -Z^*_{yx}$ was observed for SGP (0.845) and NF (0.875). This makes Ti2 comparatively more anisotropic than the Na atom. The dissimilarity in Z^* of the two Ti ions is due to hetero-ferroactive disorder at both the A and B sites in NBT, which gives rise to the relaxor behavior of NBT.[41]

The eigenvalues of the effective charge tensor vary from −1.387 to −5.306 for SGP and −1.121 to −4.887 for NF. Such a significant deviation from the ideal ionic value −2 indicates that the O atoms favor covalent bonding.

Compared to Bi and Ti, a nominal deviation of effective charge in the Na atom reflects that the Na–O bonds in NBT are mostly ionic in nature. Considering a significantly higher Born effective charge of the Bi and Ti atoms for the SGP sample compared to the NF, it can be concluded that the SGP showed a higher covalency than the NF. This nature of the Bi–O bonds and Ti–O bonds for SGP and NF is shown in Fig. 8. In this figure, due to the presence of higher covalency for the SGP sample, the electrons sharing is stronger for the Ti–O and Bi–O electronic clouds, which can be understood from the higher overlapped regions. The weaker hybridization (weak covalency and high ionicity) of Bi–O and Ti–O indicates a weaker bond strength for the NF than the SGP. This was also observed in the higher average A-O and B–O bond length or lesser bond strength for the nanofibers [A–O$_{avg}$: 2.761 67 (5) Å, B–O$_{avg}$: 1.955 19 (5) Å] than the SGP [A–O: 2.757 76 (5) Å, B–O: 1.949 67 (7) Å] from the XRD study. Hence, the elongation of the NBT lattice along the z axis (NF) weakened the covalency. The lesser covalency in the nanofibers is responsible for obtaining a lesser spontaneous polarization than the SGP NBT.[42–44] It can be inferred that the experimentally observed lesser intense Raman spectra for the NF than the SGP for the Ti–O and TiO$_6$ phonon modes are the consequence of the decreased polarizability of the Ti atoms.[45]

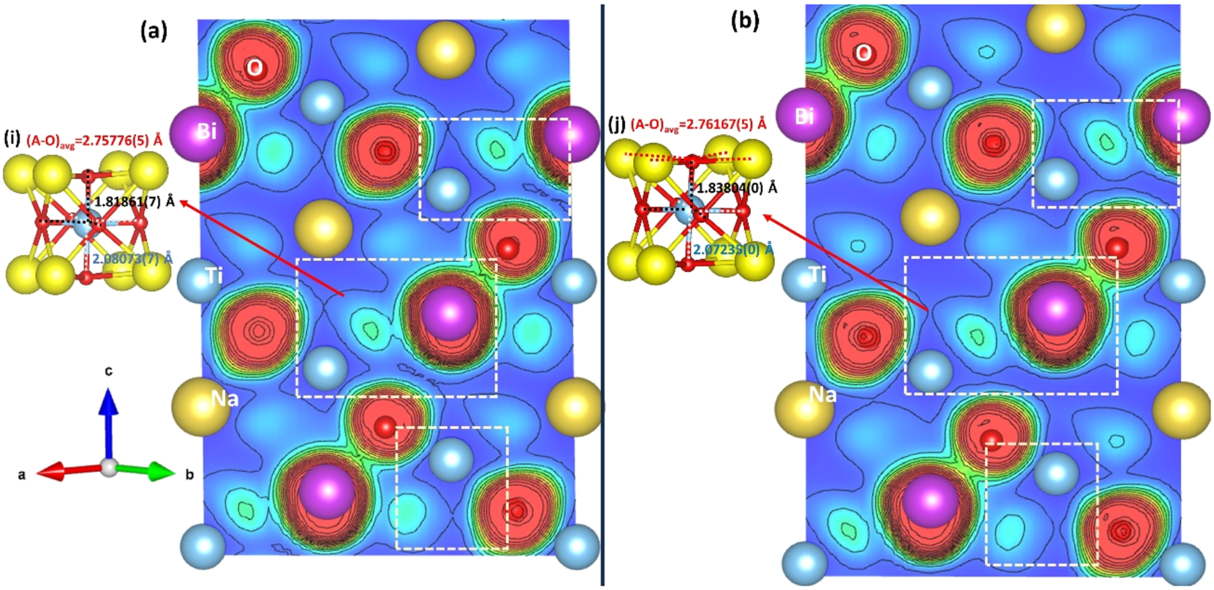

FIG. 8. Electron localization function (ELF) plot for NBT in the (110) plane for (a) SGP and (b) uniaxially elongated NBT (NF) [experimentally obtained Ti–O bond lengths and average A–O bond lengths using XRD analysis for (i) SGP and (ii) NF].

TABLE III. Elastic stiffness constants for SGP and for z-elongated structure (NF) of NBT (in GPa).

Sample	C_{11}	C_{12}	C_{13}	C_{14}	C_{33}	C_{44}	C_{66}
SGP	229.5	97.03	48.26	−22.15	153.54	27.54	66.23
NF	152.2	54.25	−2.20	22.62	71.27	−43.22	48.96

Piezoelectric properties

To understand piezo-phototronic coupling in nanofibers (NF) compared to the SGP, various parameters such as elastic constants, piezoelectric stress coefficients, and piezoelectric strain coefficients were calculated. Various mechanical properties such as stiffness, ductility, stability, and type of bonds can be determined from the elastic stiffness constants (C_{ijkl}).[46] NBT structure belongs to a trigonal space group (161) with a point group of "3*m*." The stiffness tensor (C_{ijkl}) was calculated from $C_{ijkl} = \frac{\partial^2 E}{\partial \delta_{ij} \partial \delta_{kl}}$, where E is the total energy, δ_{ij} is the stress tensor, and δ_{kl} is the strain tensor.[47] The calculated C_{mn} (i, j, k, l = 1, 2, 3; m, n = 1 to 6) values are presented in Table III.

The elastic stiffness C_{11} and C_{33} indicate the compressive stiffness (compressive stress with respect to the strain in the same axis) along the [100] and [001] directions, respectively. The constants C_{44} and C_{66} describe the shear stiffness in a plane (stress with respect to the strain across a face).[48] The C_{12}, C_{13}, and C_{14} represent the modulus for dilation on compression (axial stress with respect to the strain perpendicular to the axis). The unidirectional elastic stiffness of NF shows a lesser value (152.2, 71.27) than the SGP (229.5, 153.54). Hence, the uniaxial stiffness of the SGP is about ∼1.50 (C_{11}) and ∼2.15 (C_{33}) times larger than the NF. The larger the stiffness constant, the less flexible the materials are. Hence, the nanofibers (NF) are more uniaxially flexible than the SGP. It seems that the flexibility of the materials is advantageous to the piezo-phototronic coupling effect.[49]

The lack of inversion symmetry in the NBT structure results in intriguing piezoelectric properties. The piezoelectric stress coefficient (e_{ij}) is the total stress due to two contributions, namely, the ionic and electronic (Figs. S13–S16). The ionic contribution represents the additional internal relaxation of the relative atomic coordinates induced by the strain. The electronic contribution to the structure comes from the modifications in the local fields and is dependent on external factors. In these samples, the ionic contribution dominates for both nanofibers and SGP. According to the crystal symmetry, four piezoelectric stress coefficients are important: e_{31}, e_{33}, e_{15}, and e_{22}. Among these four stress coefficients, e_{22} is the uniaxial stress along [010] direction, while e_{33} is the uniaxial stress along [001] direction, e_{31} is the stress perpendicular to [001] direction, and e_{15} is the shear stress.

The uniaxial stress coefficient e_{22} reveals an opposite contribution from their corresponding ionic and electronic components, reducing the effective e_{22}. Moreover, the effect of ionic is negative in the SGP (−1.907 16) and positive in nanofiber (1.090 94), while the effect of electronic is positive in the SGP (0.205 72) and negative in nanofiber (−0.242 27). The net contributions in e_{22} are negative in the SGP but positive in nanofiber (Table IV).

However, the internal strain (ionic) and the electronic contributions have the same sign for the other three stress coefficients. This enhances the net stress coefficients. Among these three, e_{31} and e_{33} are positive for both samples, while e_{15} is negative. The magnitudes of all the stress coefficients are lesser in nanofibers in comparison with the SGP, which is the consequence of the calculated Born effective charges.[50]

The piezoelectric strain coefficient d_{ij} can be directly related to the piezoelectric stress coefficient e_{ik} and elastic compliance $S_{jk} = C_{jk}^{-1}$ by the relation; $d_{ij} = \sum_{k=1}^{6} e_{ik} S_{jk}$.[51] Under the uniaxial strain along the z axis, the important parameters are d_{31} and d_{33}. The *d*-matrix for both samples is represented in 3D and 2D plots using MTEX to visualize the piezoelectric strain (Fig. 9).[52,53] Four lobes represent the piezoelectric strain matrix. Along the x-y plane, three lobes are on the same plane, while the fourth is along the z axis relative to these three lobes. However, this 3D representation of the *d*-matrix appears opposite in orientation for the SGP and NF [Figs. 9(a) and 9(d)]. The reason behind such an opposite orientation comes from the opposite signs of the shear strain (d_{15}). It should be noted that the other three uniaxial strains are all positive for both samples. In addition, it is noteworthy that the d_{31} and d_{33} values are significantly large for the NF than the SGP.

Analyzing the 3D plot, one can obtain a 2D representation along the basal plane showing two halves of the spheres, one along the +z-axis and the other along the −z-axis. These are shown in Figs. 9(b), 9(c), 9(e), and 9(f). It should be noted that the reversal of the lobes is well represented by the opposite signs (colors). In the case of SGP and NF, the piezoelectric strain is much more intense in the x-y plane compared to that along the z axis, i.e., a higher strain is generated along the x-y plane. The strain is intense on the x-y plane and along the z axis for the nanofibers. The piezoelectric strain along the +z-axis for the SGP and NF is positive, and the magnitude of the NF (44.71) is higher than that of the SGP (22.63). Along the −z axis, a similar piezoelectric strain with a negative sign was observed for both SGP and NF. However, the nanofiber showed a higher value (44.71) than the SGP (22.63). The calculated d_{33} value

TABLE IV. Calculated e_{ij} and d_{ij} matrix elements for the SGP and NF.

	e_{ij} (matrix elements) (C/m^2)				d_{ij} (matrix elements) (pC/N)			
Sample	e_{31}	e_{33}	e_{15}	e_{22}	d_{31}	d_{33}	d_{15}	d_{22}
SGP	2.304 07	3.832 88	−0.799 79	−1.701 44	3.71	22.63	268.83	58.1
NF	1.943 06	3.142 89	−0.166 07	0.848 67	9.89	44.71	257.94	52.24

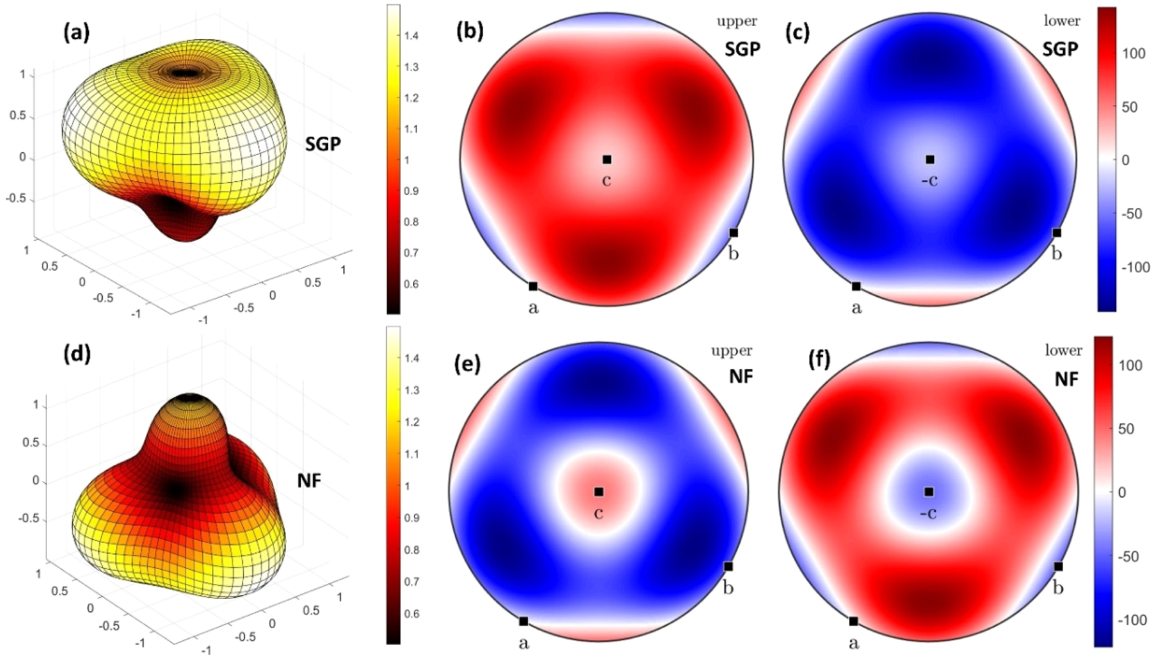

FIG. 9. (a) 3D representation of the piezoelectric strain tensor for SGP, (b) 2D representation of the upper half of the sphere for SGP, (c) 2D representation of the lower half of the sphere for SGP, (d) 3D representation of the piezoelectric strain tensor for NF, (e) 2D representation of the upper half of the sphere for NF, and (f) 2D representation of the lower half of the sphere for NF. [The tensor was plotted in MTEX considering point group 3 m (X | *a*, Y | *b*, Z | *c*)].

for SGP is similar to other reports.[46] The piezoelectric strain coefficients are ~1.97 (d_{33}) and ~2.66 (d_{31}) times higher for the NF than the SGP (Table IV). It is important to note that such enhanced d_{33} and d_{31} values for the nanofibers are due to the enhanced flexibility compared to the SGP.

In a piezoelectric material, applying stress induces uniform polarization across the crystal, generating charges on its surfaces. In a closed circuit, this surface charge movement results in a current flow when stress is applied to the piezoelectric. Hence, as per the direct piezoelectric effect, the electrical polarization vector (P_i) is given by $P_i = d_{ij}\sigma_j(i = 1, 2, 3;\ j = 1, 2, \ldots, 6)$, where σ_j is the applied stress.[48] In the case of piezo-phototronic coupling using an ultrasonic cleanser vibration, the catalyst experiences the stress produced by the mechanical vibration. According to Wu *et al.*, ultrasonic wavelengths can produce acoustic pressure with fluctuating waveforms in the range of 10^5–10^6 Pa.[12] As both the SGP and nanofibers (NF) experienced the same stress under ultrasonication, the piezoelectric strain coefficient "d_{ij}"is the deciding factor for the NF to generate a larger piezoelectric polarization compared to the SGP. As the d_{3j} elements are much higher for the NFs compared to the SGPs, the piezoelectric polarization along the z axis will be much higher for the nanofiber. A larger piezoelectric polarization is responsible for a larger inbuilt potential in a piezoelectric material, improving the surface's charge separation. Therefore, the higher polarization in the nanofibers facilitates higher charge separation, thereby reducing the recombination of the e-hole pair, which ultimately enhances the catalytic performance.

CONCLUSION

The piezo-phototronic performance was higher for the electrospun nanofibers than the sol-gel prepared particles under all three illumination conditions of 11, 250 W UV, and natural sunlight. In addition, the nanofibers showed an enhanced rate constant (k) of ~2.5–3.75 times, while the sol-gel prepared samples showed only ~1.3–1.4 times higher performance in the presence of ultrasonication compared to only photocatalysis. The improved performance was studied using a first principle study for sol-gel prepared NBT and z-elongated NBT (nanofiber). It was calculated that the elastic moduli (C_{33}) for the nanofibers was ~2.15 times lesser for the sol-gel prepared sample. This indicated that the fibers possess higher flexibility than the sol-gel particles. However, the piezoelectric stress coefficients (e_{31} and e_{33}) were ~1.2 times lesser for the nanofibers than the sol-gel particle, resulting from a lesser Born-effective charge for the fibers. The Born-effective charges revealed that due to the z-elongation in the nanofibers, the covalency in the Bi–O and Ti–O bonds was reduced, which reduced the spontaneous polarization in the nanofibers compared to the sol-gel NBT particles. The consequence was also observed in the reduction of A–O and B–O bond strengths or increase in bond lengths studied from XRD. In addition, the reduction in the Raman intensity for the Ti–O and TiO_6 vibrations resulted from decreasing covalency or spontaneous polarization in the nanofibers. However, the piezoelectric strain coefficients increased ~2.66 times and ~1.97 times for the nanofibers compared to the sol-gel particles. Such an increase was due to the higher flexibility of the fibers, which consequently enhanced the piezoelectric polarization in the nanofibers compared to the sol-gel particles of NBT. This enhanced piezoelectric polarization improved the piezo-phototronic coupling in the nanofibers. These findings suggest that electrospun nanofibers have significant potential for use in applications requiring a combination of mechanical flexibility and efficient piezo-phototronic responses.

SUPPLEMENTARY MATERIAL

The supplementary material file contains Rietveld refinement fitting and Raman spectra fitting of both SGP and NF samples. The HRTEM images and elemental compositions are also provided. The XPS plots and its detailed explanation are provided in the supplementary material file. The time resolved absorbance spectra for all illumination conditions for both samples are also given. The DFT calculated band diagrams for all compressive and expansion conditions are presented. The as calculated elastic moduli and piezoelectric stress tensors are provided in the supplementary material file. The calculated Born effective charges are tabulated in the supplementary material file.

ACKNOWLEDGMENTS

The authors K.S.S. and M.P. acknowledge the Ministry of Education, India, for providing the Prime Minister Research Fellowship (PMRF). The author S.S. acknowledges the Department of Science and Technology (DST), Government of India, for funding through Grant No. DST/TDT/AMT/2017/200. The authors also acknowledge the Department of Science and Technology (DST), Government of India, New Delhi, India, for providing FIST (Grant No. SR/FST/PSI-225/2016) instrumentation fund to the discipline of Physics, IIT Indore, to purchase a Raman Spectrometer. The authors also acknowledge the Sophisticated Instrument Center (SIC) facilities for providing the FESEM facility at IIT Indore. A. Mekki, K. Harrabi, and S. Sen acknowledge the support of the King Fahd University of Petroleum and Minerals, Saudi Arabia, under the Grant No. DF191055 DSR project.

AUTHOR DECLARATIONS

Conflict of Interest

The authors have no conflicts to disclose.

Author Contributions

Koyal Suman Samantaray: Conceptualization (lead); Data curation (lead); Formal analysis (lead); Funding acquisition (supporting); Investigation (lead); Methodology (lead); Resources (supporting); Visualization (equal); Writing – original draft (lead). **Sourabh Kumar**: Conceptualization (equal); Formal analysis (equal); Investigation (equal); Software (lead); Writing – original draft (supporting). **Maneesha P**: Formal analysis (supporting). **Dilip Sasmal**: Formal analysis (supporting); Software (supporting). **Suresh Chandra Baral**: Formal analysis (supporting). **B. R. Vaishnavi Krupa**: Data curation (supporting). **Arup Dasgupta**: Resources (supporting). **A. Mekki**: Data curation (supporting); Funding acquisition (supporting); Resources (supporting). **K. Harrabi**: Data curation (supporting); Funding acquisition (supporting); Resources (supporting). **Somaditya Sen**: Funding acquisition (equal); Project administration (lead); Resources (equal); Supervision (lead); Validation (equal); Visualization (equal); Writing – review & editing (equal).

DATA AVAILABILITY

The data that support the findings of this study are available on request from the corresponding author.

REFERENCES

[1] L. Pan, S. Sun, Y. Chen, P. Wang, J. Wang, X. Zhang, J. Zou, and Z. L. Wang, "Advances in piezo-phototronic effect enhanced photocatalysis and photoelectrocatalysis," Adv. Energy Mater. **10**(15), 2000214 (2020).

[2] S. Tu, Y. Guo, Y. Zhang, C. Hu, T. Zhang, T. Ma, and H. Huang, "Piezocatalysis and piezo-photocatalysis: Catalysts classification and modification strategy, reaction mechanism, and practical application," Adv. Funct. Mater. **30**(48), 2005158 (2020).

[3] Y. Cheng, Y. Zhang, Z. Wang, R. Guo, J. You, and H. Zhang, "Review of Bi-based catalysts in piezocatalytic, photocatalytic and piezo-photocatalytic degradation of organic pollutants," Nanoscale **15**(46), 18571–18580 (2023).

[4] D. Tan, Y. Xiang, Y. Leng, and Y. Leng, "On the metal/ZnO contacts in a sliding-bending piezoelectric nanogenerator," Nano Energy **50**, 291–297 (2018).

[5] T. Lv, J. Li, N. Arif, L. Qi, J. Lu, Z. Ye, and Y.-J. Zeng, "Polarization and external-field enhanced photocatalysis," Matter **5**(9), 2685–2721 (2022).

[6] B. Dai, G. M. Biesold, M. Zhang, H. Zou, Y. Ding, Z. L. Wang, and Z. Lin, "Piezo-phototronic effect on photocatalysis, solar cells, photodetectors and light-emitting diodes," Chem. Soc. Rev. **50**(24), 13646–13691 (2021).

[7] X. Liu, L. Xiao, Y. Zhang, and H. Sun, "Significantly enhanced piezo-photocatalytic capability in $BaTiO_3$ nanowires for degrading organic dye," J. Materiomics **6**(2), 256–262 (2020).

[8] L. Qifeng, M. Jingjun, M. Sharma, and R. Vaish, "Photocatalytic, piezocatalytic, and piezo-photocatalytic effects in ferroelectric $(Ba_{0.875}Ca_{0.125})(Ti_{0.95}Sn_{0.05})O_3$ ceramics," J. Am. Ceram. Soc. **102**(10), 5807–5817 (2019).

[9] Z. Zhao, L. Wei, S. Li, L. Zhu, Y. Su, Y. Liu, Y. Bu, Y. Lin, W. Liu, and Z. Zhang, "Exclusive enhancement of catalytic activity in $Bi_{0.5}Na_{0.5}TiO_3$ nanostructures: New insights into the design of efficient piezocatalysts and piezo-photocatalysts," J. Mater. Chem. A **8**(32), 16238–16245 (2020).

[10] R. Guo, M. Liu, Y. Xing, T. Bai, C. Zhao, H. Huang, and H. Zhang, "Piezoelectrically enhanced photocatalysis of $K_xNa_{1-x}NbO_3$ (KNN) microstructures for efficient water purification," Nanoscale **15**(15), 6920–6933 (2023).

[11] R. Djellabi, M. F. Ordonez, F. Conte, E. Falletta, C. L. Bianchi, and I. Rossetti, "A review of advances in multifunctional $XTiO_3$ perovskite-type oxides as piezo-photocatalysts for environmental remediation and energy production," J. Hazard. Mater. **421**, 126792 (2022).

[12] J. Wu, N. Qin, and D. Bao, "Effective enhancement of piezocatalytic activity of $BaTiO_3$ nanowires under ultrasonic vibration," Nano Energy **45**, 44–51 (2018).

[13] K. S. Samantaray, P. Maneesha, R. Saha, K. Harrabi, A. Mekki, and S. Sen, "Composition and electric field driven studies on modified NBT-based lead-free ceramics," Mater. Sci. Eng.: B **300**, 117140 (2024).

[14] B. N. Rao, A. N. Fitch, and R. Ranjan, "Ferroelectric–ferroelectric phase coexistence in $Na_{1/2}Bi_{1/2}TiO_3$," Phys. Rev. B **87**(6), 060102 (2013).

[15] A. Verma, A. K. Yadav, S. Kumar, V. Srihari, R. Jangir, H. K. Poswal, S. Biring, and S. Sen, "Enhanced energy storage properties in A-site substituted $Na_{0.5}Bi_{0.5}TiO_3$ ceramics," J. Alloys Compd. **792**, 95–107 (2019).

[16] X. Zhou, Q. Sun, D. Zhai, G. Xue, H. Luo, and D. Zhang, "Excellent catalytic performance of molten-salt-synthesized $Bi_{0.5}Na_{0.5}TiO_3$ nanorods by the piezo-phototronic coupling effect," Nano Energy **84**, 105936 (2021).

[17] D. Liu, Y. Song, Z. Xin, G. Liu, C. Jin, and F. Shan, "High-piezocatalytic performance of eco-friendly $(Bi_{1/2}Na_{1/2})TiO_3$-based nanofibers by electrospinning," Nano Energy **65**, 104024 (2019).

[18] J. Ji, Y. Pu, L. Chang, T. Ouyang, P. Wang, C. He, and S. Zhou, "Boosting the separation of bulk charge in $Na_{0.5}Bi_{0.5}TiO_3$ by the synergetic effect of ferroelectric polarization and thin-sheet shape," Ceram. Int. **47**(19), 27650–27659 (2021).

[19] M. B. Ghasemian, Q. Lin, E. Adabifiroozjaei, F. Wang, D. Chu, and D. Wang, "Morphology control and large piezoresponse of hydrothermally synthesized lead-free piezoelectric $(Bi_{0.5}Na_{0.5})TiO_3$ nanofibres," RSC Adv. **7**(25), 15020–15026 (2017).

[20] D.-M. Liu, J.-T. Zhang, C.-C. Jin, B.-B. Chen, J. Hu, R. Zhu, and F. Wang, "Insight into oxygen-vacancy regulation on piezocatalytic activity of $(Bi_{1/2}Na_{1/2})TiO_3$ crystallites: Experiments and first-principles calculations," Nano Energy **95**, 106975 (2022).

[21] Y. Zhang, W. Jie, P. Chen, W. Liu, and J. Hao, "Ferroelectric and piezoelectric effects on the optical process in advanced materials and devices," Adv. Mater. **30**(34), 1707007 (2018).

[22] X. Wei, N. Domingo, Y. Sun, N. Balke, R. E. Dunin-Borkowski, and J. Mayer, "Progress on emerging ferroelectric materials for energy harvesting, storage and conversion," Adv. Energy Mater. **12**(24), 2201199 (2022).

[23] H. D. Megaw and C. N. W. Darlington, "Geometrical and structural relations in the rhombohedral perovskites," Acta Cryst. A **31**(2), 161–173 (1975).

[24] E. Kroumova, M. I. Aroyo, J. M. Perez-Mato, A. Kirov, C. Capillas, S. Ivantchev, and H. Wondratschek, "Bilbao crystallographic server: Useful databases and tools for phase-transition studies," Phase Transitions **76**(1–2), 155–170 (2003).

[25] D. Maurya, V. Petkov, A. Kumar, and S. Priya, "Nanostructured lead-free ferroelectric $Na_{0.5}Bi_{0.5}TiO_3$–$BaTiO_3$ whiskers: Synthesis mechanism and structure," Dalton Trans. **41**(18), 5643 (2012).

[26] L. Yang and B. Kruse, "Revised Kubelka–Munk theory. I. Theory and application," J. Opt. Soc. Am. A **21**(10), 1933 (2004).

[27] J. H. Nobbs, "Kubelka–Munk theory and the prediction of reflectance," Rev. Prog. Color. Relat. Top. **15**(1), 66–75 (2008).

[28] C. He, C. Deng, J. Wang, X. Gu, T. Wu, K. Zhu, and Y. Liu, "Crystal orientation dependent optical transmittance and band gap of $Na_{0.5}Bi_{0.5}TiO_3$–$BaTiO_3$ single crystals," Physica B **483**, 44–47 (2016).

[29] S. Zaynobidinov, R. G. Ikramov, and R. M. Jalalov, "Urbach energy and the tails of the density of states in amorphous semiconductors," J. Appl. Spectrosc. **78**(2), 223–227 (2011).

[30] A. Kumar, "A review on the factors affecting the photocatalytic degradation of Hazardous materials," Mater. Sci. Eng. Int. J. **1**(3), 106 (2017).

[31] S. Zhu and D. Wang, "Photocatalysis: Basic principles, diverse forms of implementations and emerging scientific opportunities," Adv. Energy Mater. **7**(23), 1700841 (2017).

[32] S. C. Baral, P. Maneesha, S. Datta, K. Dukiya, D. Sasmal, K. S. Samantaray, V. K. Br, A. Dasgupta, and S. Sen, "Enhanced photocatalytic degradation of organic pollutants in water using copper oxide (CuO) nanosheets for environmental application," JCIS Open **13**, 100102 (2024).

[33] R. Qian, H. Zong, J. Schneider, G. Zhou, T. Zhao, Y. Li, J. Yang, D. W. Bahnemann, and J. H. Pan, "Charge carrier trapping, recombination and transfer during TiO_2 photocatalysis: An overview," Catal. Today **335**, 78–90 (2019).

[34] H. Wang, L. Zhang, Z. Chen, J. Hu, S. Li, Z. Wang, J. Liu, and X. Wang, "Semiconductor heterojunction photocatalysts: Design, construction, and photocatalytic performances," Chem. Soc. Rev. **43**(15), 5234 (2014).

[35] B. Ohtani, "Titania photocatalysis beyond recombination: A critical review," Catalysts **3**(4), 942–953 (2013).

[36] Z. Liu, X. Yu, and L. Li, "Piezopotential augmented photo- and photoelectrocatalysis with a built-in electric field," Chin. J. Catal. **41**(4), 534–549 (2020).

[37] J. Yuan, X. Huang, L. Zhang, F. Gao, R. Lei, C. Jiang, W. Feng, and P. Liu, "Tuning piezoelectric field for optimizing the coupling effect of piezo-photocatalysis," Appl. Catal., B **278**, 119291 (2020).

[38] P. Ghosez, J. P. Michenaud, and X. Gonze, "The physics of dynamical atomic charges: The case of ABO_3 compounds," Phys. Rev. B **58**(10), 6224–6240 (1998).

[39] X. N. Zhu, X. Chen, H. Tian, and X. M. Chen, "Atomic scale investigation of enhanced ferroelectricity in (Ba, Ca)TiO_3," RSC Adv. **7**(36), 22587–22591 (2017).

[40] J. Pan, M. K. Niranjan, and U. V. Waghmare, "Aliovalent cation ordering, coexisting ferroelectric structures, and electric field induced phase transformation in lead-free ferroelectric $Na_{0.5}Bi_{0.5}TiO_3$," J. Appl. Phys. **119**(12), 124102 (2016).

[41] M. K. Niranjan, T. Karthik, S. Asthana, J. Pan, and U. V. Waghmare, "Theoretical and experimental investigation of Raman modes, ferroelectric and dielectric properties of relaxor $Na_{0.5}Bi_{0.5}TiO_3$," J. Appl. Phys. **113**(19), 194106 (2013).

[42] C.-Z. Wang, R. Yu, and H. Krakauer, "Polarization dependence of Born effective charge and dielectric constant in $KNbO_3$," Phys. Rev. B **54**(16), 11161–11168 (1996).

[43] A. Dal Corso, M. Posternak, R. Resta, and A. Baldereschi, "*Ab initio* study of piezoelectricity and spontaneous polarization in ZnO," Phys. Rev. B **50**(15), 10715–10721 (1994).

[44] M. Posternak, R. Resta, and A. Baldereschi, "Role of covalent bonding in the polarization of perovskite oxides: The case of $KNbO_3$," Phys. Rev. B **50**(12), 8911–8914 (1994).

[45] G. Keresztury, "Raman spectroscopy: Theory," in *Handbook of Vibrational Spectroscopy*, 1st ed., edited by J. M. Chalmers and P. R. Griffiths (Wiley, 2001).

[46] O. Mezilet, A. Assali, S. Meskine, A. Boukortt, and M. S. Halati, "New insights into the piezoelectric, thermodynamic and thermoelectric properties of lead-free ferroelectric perovskite $Na_{0.5}Bi_{0.5}TiO_3$ from *Ab initio* calculations," Mater. Today Commun. **31**, 103371 (2022).

[47] Y. Pan, "The structural, mechanical and thermodynamic properties of the orthorhombic TMAl (TM = Ti, Y, Zr, and Hf) aluminides from first-principles calculations," Vacuum **181**, 109742 (2020).

[48] J. F. Nye, *Physical Properties of Crystals: Their Representation by Tensors and Matrices* (Clarendon Press Oxford University Press, Oxford [Oxfordshire], New York, 1984) 1st Published in Pbk. With Corrections, 1984.

[49] X. Wang, X. Gao, M. Li, S. Chen, J. Sheng, and J. Yu, "Synthesis of flexible $BaTiO_3$ nanofibers for efficient vibration-driven piezocatalysis," Ceram. Int. **47**(18), 25416–25424 (2021).

[50] P. Hermet, "First-principles based analysis of the piezoelectric response in α-$LiIO_3$," Comput. Mater. Sci. **138**, 199–203 (2017).

[51] S. Konabe and T. Yamamoto, "Piezoelectric coefficients of bulk 3R transition metal dichalcogenides," Jpn. J. Appl. Phys. **56**(9), 098002 (2017).

[52] D. Mainprice, F. Bachmann, R. Hielscher, H. Schaeben, and G. E. Lloyd, "Calculating anisotropic piezoelectric properties from texture data using the MTEX open source package," Mater. Sci., Phys., Eng. **409**(1), 223–249 (2015).

[53] M. De Jong, W. Chen, H. Geerlings, M. Asta, and K. A. Persson, "A database to enable discovery and design of piezoelectric materials," Sci. Data **2**(1), 150053 (2015).